






# Transferability of the chemical-bond-based machine learning model for dipole moment: The GHz to THz dielectric properties of liquid propylene glycol and polypropylene glycol

Tomohito Amano <sup>1</sup>, Tamio Yamazaki <sup>2</sup>, Naoki Matsumura <sup>3</sup>, Yuta Yoshimoto <sup>3</sup>, and Shinji Tsuneyuki <sup>1,4</sup>

<sup>1</sup>*Department of Physics, The University of Tokyo, Hongo, Bunkyo-ku, Tokyo 113-0033, Japan*

<sup>2</sup>*JSR-UTokyo Collaboration Hub, CURIE, JSR Corporation, 1-9-2, Higashi-Shinbashi, Minato-ku, Tokyo 105-8640, Japan*

<sup>3</sup>*Fujitsu Research, Fujitsu Limited, 4-1-1, Kamiodanaka, Nakahara-ku, Kawasaki, Kanagawa 211-8588, Japan*

<sup>4</sup>*Institute for Physics of Intelligence, The University of Tokyo, Hongo, Bunkyo-ku, Tokyo 113-0033, Japan*



(Received 29 October 2024; revised 13 February 2025; accepted 26 March 2025; published 24 April 2025)

We conducted a first-principles study of the dielectric properties of liquid propylene glycol (PG) and polypropylene glycol (PPG) using a recently developed chemical-bond-based machine learning (ML) model for dipole moments [T. Amano *et al.*, *Phys. Rev. B* **110**, 165159 (2024)]. The ML dipole models successfully predict the dipole moment of various liquid configurations in close agreement with density functional theory calculations, and they generate 20 ns quantum-accuracy dipole moment trajectories to calculate the dielectric function, when combined with ML potentials. The calculated dielectric function of PG closely matches experimental results. We identified a libration peak at  $600\text{ cm}^{-1}$  and an intermolecular mode at  $100\text{ cm}^{-1}$ , previously noted experimentally. Furthermore, the models trained on PG2 training data can apply to longer chain PPGs not included in the training data. The present research marks the first step toward developing a universal bond-based dipole model.

DOI: [10.1103/PhysRevB.111.165149](https://doi.org/10.1103/PhysRevB.111.165149)

## I. INTRODUCTION

Computational simulations of dielectric functions are essential for understanding the dynamical, structural, and optical properties of materials. The first-principles anharmonic phonon method [1,2] is used to calculate the lattice dielectric properties of crystalline systems, whereas molecular dynamics (MD) simulations are commonly employed for liquid substances [3,4]. The dielectric function, which is derived from the dipole autocorrelation function along MD trajectories, requires both accurate trajectory data and precise estimation of the dipole moments of the system. In classical MD simulations, empirical fixed charges are typically used to calculate the dipole moment. However, this approach does not account for local atomic polarization effects, sometimes making it challenging to quantitatively reproduce experimental results [5–7]. The classical polarizable force fields and first-principles molecular dynamics are known methods for incorporating the effects of polarization due to many-body atomic interactions. Notable examples of the former include the Drude oscillator model [8] and the induced dipole model [9], which have been successfully applied to the calculation of dielectric constants [4] and dielectric functions [10,11] of molecular systems.

The *ab initio* molecular dynamics (AIMD) simulations [12], which incorporate many-body atomic interactions based on quantum electronic structure calculations, have been extensively used to study the dielectric properties of various materials [13–15]. A key advantage of the AIMD method is that the electronic polarization effects can be directly analyzed in a quantum-mechanical manner through the maximally

localized Wannier function (MLWF) method [16–18]. Several AIMD studies on molecular liquids have revealed that the polarization of the Wannier functions (WFs), caused by the local atomic interactions, enhances the dipole moments compared to the gas phase [13,19] and has a significant effect on the absorption spectrum in the terahertz (THz) to infrared (IR) regions [5]. Unfortunately, the high computational cost of AIMD restricts its typical applications to systems with only hundreds of atoms and a timescale of 100 ps, which is insufficient to study the dielectric properties of large molecules.

To achieve the accuracy of first-principles calculations and the efficiency of empirical force fields, various ML force fields have been actively developed [20–24]. Alongside ML potentials, ML models for atomic partial charges have also been developed to study dielectric properties [25–28] and to model electrostatic potentials [29–35]. Unlike empirical fixed charges, ML partial charges dynamically change their values according to the surrounding atomic environment, thereby more accurately capturing local structural features.

A different approach, in line with the modern theory of polarization [16], is to directly predict Wannier centers (WCs), which represent the mass center of WFs [7,36–39]. Several authors introduced the Wannier centroid, defined as the average position of the WCs in a molecule, and constructed the ML models of the centroid to investigate the dielectric properties of  $\text{H}_2\text{O}$  [36–39]. The centroid approach was also successfully applied to study the dielectric properties of crystalline systems including  $\text{BaPbO}_3$  [40] and  $\text{KH}_2\text{PO}_4$  [41]. Furthermore, ML molecular dipole moment methods have been developed by combining Wannier centroids and ionic charges [42,43]. Additionally, ML-predicted WCs play an

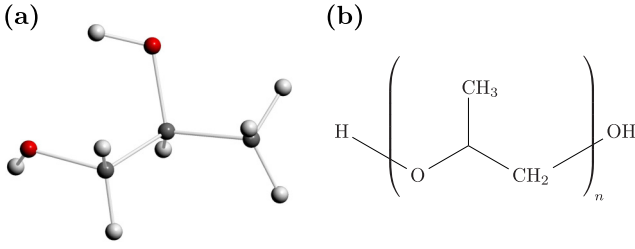


FIG. 1. (a) The molecular structure of PG. The red, gray, and white spheres represent oxygen, carbon, and hydrogen atoms, respectively. (b) SMILES of PPG, with  $n = 1$  corresponding to PG. In this work,  $n = 2$ –12 were used.

important role in describing long-range interactions in ML force fields [39,44,45].

However, methods that predict centroids or molecular dipoles often require larger cutoffs for ML descriptors when applied to molecules with higher molecular weights. To address this challenge, we recently developed a chemical-bond-based ML model for WC [46], which assigns WCs to chemical bonds and predicts the WC for each chemical bond rather than the entire molecule. This method enables accurate dipole moment predictions without compromising precision, even for large molecules. Since the positions of the WCs do not vary significantly between different molecular species, the bond-based ML dipole models are potentially transferable across various materials. As the previous study only reported the results for methanol and ethanol, it is desirable to investigate the transferability of the proposed ML scheme in application to more complex molecules. Moreover, it is essential to explore the dielectric properties in frequency ranges that are inaccessible to AIMD by combining this method with ML potentials, which was not addressed in the previous study.

We selected propylene glycol (PG), also known as 1,2-propanediol, along with its oligomers, polypropylene glycol (PPG), to validate the transferability of our bond-based ML approach. PG, whose structure is depicted in Fig. 1, is a well-known glass-forming liquid with a glass transition temperature of approximately 170 K [47,48]. The dielectric properties in both the liquid and glass phases are extensively examined through various experiments [49–51]. PPG has also been thoroughly studied for its dielectric properties, including dimer (PG2) [52], trimer (PG3) [53,54], PPG425 (PG7) [55,56], PPG725 (PG12) [57], and larger polymers [58,59]. The notation PG $n$  refers to the corresponding  $n$ -mer of PG, and PPG725 indicates a molecular weight of 725. Although many theoretical studies on PG have relied on classical MD simulations [3,60–62], challenges remain in the accurate prediction of dielectric properties. The optimized potential for liquid simulations (OPLS) united-atom force field [63] predicts a dielectric constant of 12 at room temperature [3], significantly underestimating the experimental value of 28 [64,65]. A specialized force field for PG [60] has not been used to investigate the dielectric properties. There is a strong demand for studies that utilize accurate first-principles methods to fully explore the dielectric properties of PG.

In this paper, we apply the bond-based ML dipole approach to PG and PPGs, demonstrating that this method can generate long-time first-principles dipole trajectories when

combined with ML potentials. Furthermore, we show that the model trained on PG2 data can be directly applied to higher molecular weight PPGs without additional fine-tuning. To perform MD simulations with first-principles accuracy, we trained ML potentials for PG and di-propylene glycol (PG2) using the DeepMD-kit [22,66]. We first studied the dielectric properties of PG using the trained ML potentials and the ML dipole models. To the best of our knowledge, this is the first detailed *ab initio* study on the dielectric properties of PG. The calculated dielectric spectrum closely matches the experimental data across a wide range of frequencies from GHz to THz regions, revealing a hydroxyl hydrogen libration peak at 600  $\text{cm}^{-1}$  and a mode at 100  $\text{cm}^{-1}$  attributed to intermolecular interactions. Subsequently, we employed the ML potentials and ML dipoles trained on PG2 to predict the dipole moment and dielectric function of higher molecular weight PPGs. Our calculations closely reproduced the experimental results, demonstrating the transferability of our ML scheme.

## II. THEORY

### A. Dipole moments

The MLWF method decomposes the total dipole moment of the system into the ionic and the electronic parts as [17,18]

$$\mathbf{M} = e \sum_{i=1}^N Z_i \mathbf{r}_i - 2e \sum_{k=1}^{N_w} \mathbf{w}_k, \quad (1)$$

where  $Z_i$  and  $\mathbf{r}_i$  are the ionic charge and nuclear position of the  $i$ th atom, respectively.  $\mathbf{w}_k$  describes the position of the  $k$ th WC.  $N$  and  $N_w$  represent the number of atoms and WCs, respectively. The factor 2 in the second term represents the spin degrees of freedom. We employ a valence-only pseudopotential method, where the nuclear charges  $eZ_i$  encompass contributions from both the nuclei and the frozen core electrons, while the WCs correspond to the valence electrons.

Following the bond dipole scheme proposed in Ref. [46], we assign each WC to oxygen lone pairs or chemical bonds. For simplicity, we consider a system consisting of carbons, oxygens, and hydrogens with single bonds. The total dipole moment in Eq. (1) can be rewritten in the bond-based form as

$$\mathbf{M} = \sum_{i=1}^{N_{\text{single}}} \boldsymbol{\mu}_i^{\text{single}} + \sum_{i=1}^{N_{\text{lp}}} \boldsymbol{\mu}_i^{\text{lp}}, \quad (2)$$

$$\boldsymbol{\mu}_i^{\text{single}} = 2e(\mathbf{r}_i^s - \mathbf{w}_i^s), \quad (3)$$

$$\boldsymbol{\mu}_i^{\text{lp}} = 4e(\mathbf{r}_i^O - \mathbf{w}_i^{\text{lp}}), \quad (4)$$

where  $\mathbf{r}_i^s$  and  $\mathbf{r}_i^O$  are the positions of the  $i$ th bond center (BC) of the chemical bonds and oxygens, and  $\mathbf{w}_i^s$  and  $\mathbf{w}_i^{\text{lp}}$  are the positions of assigned WCs.  $N_{\text{single}}$  and  $N_{\text{lp}}$  are the number of single bonds and lone pairs, respectively. We refer to  $\boldsymbol{\mu}_i^{\text{single}}$  and  $\boldsymbol{\mu}_i^{\text{lp}}$  as bond dipoles, which are simply the relative vectors from the WCs to the BCs or oxygens.

Equation (2) decomposes the dipole moment into its most fundamental components, allowing for the definition of a new virtual bond dipole by summing the contributions from arbitrary bond dipoles. Since the oxygen lone pair is thought to correlate with the WCs of the adjacent bonds, combining it

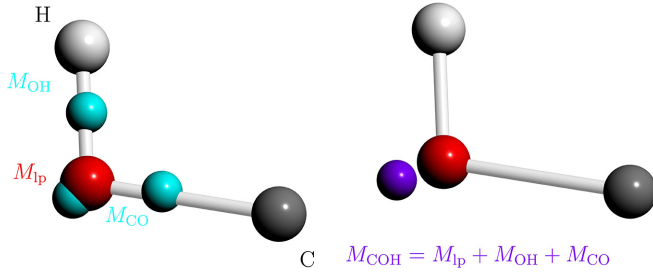


FIG. 2. The schematic images of the COH bond dipole. Left: The carbon (gray), oxygen (red), and hydrogen (white) atoms constituting the COH bond with three corresponding WCs (cyan). Right: The COH bond Wannier center (purple).

with surrounding bonds would achieve both maintaining accuracy and decreasing computational cost. We define a new bond dipole by aggregating the contributions from the lone pair  $i$  and the two adjacent bonds  $a(i)$  and  $b(i)$ . In systems consisting only of carbons, hydrogens, and oxygens, two distinct bond dipoles can be defined,  $\mu^{\text{COH}}$  and  $\mu^{\text{COC}}$ :

$$\mu_i^{\text{COH}} = \mu_{a(i)}^{\text{CO}} + \mu_i^{\text{lp}} + \mu_{b(i)}^{\text{OH}}, \quad (5)$$

$$\mu_i^{\text{COC}} = \mu_{a(i)}^{\text{CO}} + \mu_i^{\text{lp}} + \mu_{b(i)}^{\text{CO}}. \quad (6)$$

Figure 2 illustrates the concept of the COH dipole moment. The total dipole moment in Eq. (2) is rewritten in terms of CH, CC, COC, and COH bond dipole moments as

$$\mathbf{M} = \sum_{i=1}^{N_{\text{CH}}} \mu_i^{\text{CH}} + \sum_{i=1}^{N_{\text{CC}}} \mu_i^{\text{CC}} + \sum_{i=1}^{N_{\text{COC}}} \mu_i^{\text{COC}} + \sum_{i=1}^{N_{\text{COH}}} \mu_i^{\text{COH}}, \quad (7)$$

where  $N_{\text{CH}}$ ,  $N_{\text{CC}}$ ,  $N_{\text{COC}}$ , and  $N_{\text{COH}}$  are the numbers of each bond.

### B. The dielectric properties

The dielectric function  $\varepsilon(\omega)$  can be calculated by the Fourier transform of the derivative of the autocorrelation function of the dipole moment as [67]

$$\varepsilon(\omega) = \varepsilon'(\omega) - i\varepsilon''(\omega) \quad (8)$$

$$= \varepsilon^\infty - \frac{1}{3\varepsilon_0 k_B T V} \int_0^\infty \left( \frac{d\langle \mathbf{M}(0) \cdot \mathbf{M}(t) \rangle}{dt} \right) \times e^{-i\omega t} dt, \quad (9)$$

where  $\varepsilon^\infty$  is the high-frequency dielectric constant,  $k_B$  is the Boltzmann constant,  $T$  is the temperature,  $V$  is the volume of the simulation cell,  $\varepsilon_0$  is the dielectric constant in vacuum, and  $\mathbf{M}$  represents the total dipole moment of the system.  $\langle \rangle$  denotes the canonical ensemble average.  $\varepsilon'(\omega)$  and  $\varepsilon''(\omega)$  represent the real and imaginary part of the dielectric function, respectively. To avoid evaluating the derivative of the autocorrelation function, we adopt the alternative form derived through the integration by parts of Eq. (9) [68],

$$\varepsilon(\omega) = \varepsilon^0 - \frac{i\omega}{3\varepsilon_0 k_B T V} \int_0^\infty \langle \mathbf{M}(0) \cdot \mathbf{M}(t) \rangle e^{-i\omega t} dt \quad (10)$$

$$= \varepsilon^0 + \frac{1}{3\varepsilon_0 k_B T V i\omega} \int_0^\infty \langle \dot{\mathbf{M}}(0) \cdot \dot{\mathbf{M}}(t) \rangle e^{-i\omega t} dt, \quad (11)$$

where  $\varepsilon^0 = \varepsilon(0)$  is the relative static dielectric constant of a material. The imaginary part of the dielectric function is explicitly given as [15]

$$\varepsilon''(\omega) = \frac{\omega}{3\varepsilon_0 k_B T V} \text{Re} \int_0^\infty \langle \mathbf{M}(0) \cdot \mathbf{M}(t) \rangle e^{-i\omega t} dt \quad (12)$$

$$= \frac{\omega}{6\varepsilon_0 k_B T V} \int_{-\infty}^\infty \langle \mathbf{M}(0) \cdot \mathbf{M}(t) \rangle e^{-i\omega t} dt. \quad (13)$$

The absorption coefficient per unit length  $\alpha(\omega)$  is defined through Lambert-Beer's law [69]:

$$\alpha(\omega) = \frac{\omega \varepsilon''(\omega)}{c n(\omega)} \quad (14)$$

$$= \frac{\omega^2}{6\varepsilon_0 c n(\omega) k_B T V} \int_{-\infty}^\infty \langle \mathbf{M}(0) \cdot \mathbf{M}(t) \rangle e^{-i\omega t} dt, \quad (15)$$

where  $c$  is the speed of light in vacuum, and  $n(\omega)$  is the refractive index calculated from the dielectric function. Different coefficients are sometimes adopted in the literature [70,71], depending on the classical approximation applied to the Kubo formula in Eq. (9).

Similarly, we define the power spectrum  $I_x(\omega)$  of a real-valued time series  $x(t)$  as the Fourier transform of the normalized time autocorrelation function:

$$I_x(\omega) = \int_{-\infty}^\infty \frac{\langle x(0)x(t) \rangle}{\langle x(0)^2 \rangle} e^{-i\omega t} dt. \quad (16)$$

If  $\mathbf{x}(t)$  is the vector quantity, one may evaluate the inner dot of  $\mathbf{x}(t)$  as

$$I_{\mathbf{x}}(\omega) = \int_{-\infty}^\infty \frac{\langle \mathbf{x}(0) \cdot \mathbf{x}(t) \rangle}{\langle |\mathbf{x}(0)|^2 \rangle} e^{-i\omega t} dt. \quad (17)$$

A detailed analysis of MD trajectories becomes possible by considering various physical quantities, such as interatomic distances and angles for  $x$  [5,72]. One good example is the vibrational density of states (VDOS), which for the  $i$ th atom is given by the Fourier transform of the velocity autocorrelation function (VACF) as

$$D_i(\omega) = \int_{-\infty}^\infty \langle \mathbf{v}_i(0) \cdot \mathbf{v}_i(t) \rangle e^{-i\omega t} dt, \quad (18)$$

where  $\mathbf{v}_i(t)$  is the atomic velocity at time  $t$ . The total VDOS is given by averaging over all atomic contributions of Eq. (18):

$$D(\omega) = \frac{1}{N} \sum_{i=1}^N D_i(\omega). \quad (19)$$

We can calculate the VACF for each atomic species by restricting the summation.

In practice, the time integration is evaluated using the convolution of the Fourier transform. Using the Fourier-transformed atomic velocity

$$\mathbf{v}_i(\omega) = \int_{-\infty}^\infty \mathbf{v}_i(t) e^{-i\omega t} dt, \quad (20)$$

the atomic VDOS is obtained by

$$D_i(\omega) = \mathbf{v}_i^*(\omega) \cdot \mathbf{v}_i(\omega), \quad (21)$$

which is considerably faster than computing Eq. (18) directly.

### C. Machine learning model

We follow the neural network architecture proposed by Zhang *et al.* [37], which is suitable for predicting vector quantities by considering rotational symmetry. We consider a ML model that predicts the  $i$ th bond dipole  $\mu_i$  based on the input  $\mathbf{r}_k \in \mathcal{N}_i$ , where  $\mathcal{N}_i$  represents the atoms located within the cutoff radius  $r_c$  around the BC or oxygen atom  $i$ , and  $N_i$  denotes the total number of such atoms. In this approach, the atomic environments are embedded in a rotationally invariant feature matrix through a first neural network, named the embedding network, and the feature matrix is used as an input of the second neural network, called the fitting network, to predict the bond dipole moment.

Hereafter, we use a coordinate system where the origin is set at the position of the  $i$ th BC or oxygen atom, and the coordinates of the  $k$ th atom in this system are denoted as  $\mathbf{r}_{ik}$ . The following four-component vectors represent the atomic coordinates:

$$\mathbf{q}_{ik} = (q_{ik}^1, q_{ik}^2, q_{ik}^3, q_{ik}^4) \quad (22)$$

$$= s(r_{ik})(1, x_{ik}/r_{ik}, y_{ik}/r_{ik}, z_{ik}/r_{ik}), \quad (23)$$

where  $s(r)$  is the cutoff function that is equal to  $1/r'_{ki}$  in  $r'_{ki} < r_{c0}$  and decays to zero as  $r'_{ki}$  approaches  $r_c$ . The  $N_i$  by 4 matrix  $\mathbf{Q}_i = (Q_{k\lambda}) = (q_{ik}^\lambda)$ , which is explicitly written as

$$Q_i = \begin{pmatrix} q_{i1}^1, q_{i1}^2, q_{i1}^3, q_{i1}^4 \\ \vdots \\ q_{iN_i}^1, q_{iN_i}^2, q_{iN_i}^3, q_{iN_i}^4 \end{pmatrix}, \quad (24)$$

contains information about the surrounding atoms of the  $i$ th BC or oxygen atom. The atomic index  $k = 1, 2, \dots, N_i$  is sorted first based on the type of neighboring atoms, and then on the atomic distances  $q_{ik}^1$ . For each atomic type, the number up to a specified maximum number of atoms is considered. To keep the length of the descriptor constant, the descriptors with different atomic types are padded with zero if the neighbor lists of atomic species are smaller than the specified value. The embedding neural network takes only the distance information  $\{q_{ik}^1 | k = 1, \dots, N_i\}$  from  $Q_i$  as input and produces an output with  $MN_i$  elements, represented by the  $M \times N_i$  matrix  $E$ , where  $M$  is the hyperparameter. Noting the first  $M' (< M)$  rows of  $E$  as a new matrix  $E'$ , we define the feature matrix  $D_i$  as

$$\mathbf{D}_i = (\mathbf{E}\mathbf{Q}_i)(\mathbf{E}'\mathbf{Q}_i)^T = \mathbf{E}\mathbf{Q}_i\mathbf{Q}_i^T\mathbf{E}'^T, \quad (25)$$

which is an  $M \times M'$  matrix.

The fitting network takes  $D_i$  as input and produces  $M$  outputs  $F_j (j = 1, 2, \dots, M)$ , which are ultimately used to compute the bond dipoles  $\mu_i = (\mu_i^1, \mu_i^2, \mu_i^3)$  with the last three columns of  $\mathbf{T} = \mathbf{E}\mathbf{Q}$ ,

$$\mu_i^\lambda = \sum_{j=1}^M F_j(\mathbf{D})T_{j,\lambda+1} \quad (\lambda = 2, 3, 4). \quad (26)$$

## III. COMPUTATIONAL DETAILS

### A. Classical molecular dynamics simulation

We performed the classical molecular dynamics (CMD) calculations using the GROMACS package [73] to prepare

initial configurations for the ML molecular dynamics simulations. In each system, molecules were positioned in the simulation box using the PACKMOL package [74] to generate the initial configurations. The force field parameters stem from the general AMBER force field (GAFF2) [75] and the atomic charges from the AM1-BCC charge [76], respectively, with topology files generated by the Antechamber [77] and ACPYPE package [78]. The simulations were performed in an  $NVT$  ensemble at 300 K using velocity rescaling. The equations of motion were integrated using the Verlet algorithm with a 1 fs time step, which is common setup in previous CMD studies of hydrogen-bonded liquids [11,79].

### B. *Ab initio* electronic structure calculation

We employed the CPMD package v.4.3 [80] for *ab initio* electronic ground-state calculations and WC constructions to prepare ML training data. The Becke-Lee-Yang-Parr (BLYP) functional [81,82], a family of the generalized gradient approximation (GGA) scheme, was used for the exchange-correlation functional. We included Grimme's dispersion correction D2 [83] to account for van der Waals interactions. The valence-only Goedecker-Teter-Hutter (GTH) pseudopotentials [84] were used, and the plane waves represented the electronic wave functions with an energy cutoff of 100 Ry. The energy convergence criterion was set to  $1 \times 10^{-7} E_h$ . Only the  $\Gamma$ -point was considered for all calculations, which is sufficient for the supercell calculations of insulating materials [5,36,85].

### C. Training of the machine learning models

We employed the DeePMD-kit package [22] to construct neural network many-body potentials for PG and PG2. The active learning scheme implemented in the GeNNIP4MD [86] was used to generate training structures. We first prepared 3000 initial structures collected from  $NVT$  AIMD calculations at 300, 600, and 800 K, from which we trained the initial ML potentials. The initial potentials were then improved through a subsequent active sampling procedure, which includes data sampling and screening. In the sampling phase, we employed ML MD simulations to generate a diverse set of candidate structures. We carried out 100 ps simulations under both  $NVT$  and  $NPT$  ensembles at temperatures of 300, 600, and 800 K, with a constant pressure of 1 bar [87,88]. We extracted candidate structures at 100 fs intervals. We also performed nonequilibrium MD simulations to increase the accuracy and robustness of the potentials based on the volume scan technique [89]. This comprehensive sampling strategy significantly improves the stability of ML MD simulations.

In the screening phase, our objective was to refine the set of candidate structures for ML training by prioritizing novel and structurally distinct configurations that contribute to model improvement. First, we applied an ensemble-based approach, training four separate ML models with different initial seeds [90]. To further eliminate redundancy, we employed the densMAP dimensionality reduction technique [91], ensuring a more diverse and representative dataset.

We sampled 14 996 and 27 438 structures for PG and PG2, respectively, which were used as training data for the ML



potentials. We trained the ML potentials for PG and PG2 separately, and PG data were only used to train PG models, while PG2 data were only used to train PG2 models. While ML potentials with the relatively small number of training data suffer from collapsing simulations [85,92], our potentials stably perform for 20-ns-long time calculations with inclusion of the large number and wide variety of training structures through active learning. The neural network architecture includes an embedding network of three layers with 25, 50, and 100 neurons, respectively, and a fitting network with a three-layer structure, each containing 100 neurons. The dataset features and potential accuracy of PG are summarized in Appendix B.

We utilized the PyTorch-based MLWC (machine learning Wannier center) package [93] to assign WCs and construct the ML models for dipole moments of PG and PG2. We used the same structures obtained from the active learning procedure. The descriptors contained up to 24 neighboring atoms for each atomic species, with an outer cutoff of 6 Å and an inner cutoff of 4 Å. The size of the feature matrix in Eq. (25) was set to  $M = 20$  and  $M' = 6$ . For both ML potentials and dipole moments, we used 90% of the reference data for training, and the remaining 10% of the data points for validation.

#### D. Deep potential molecular dynamics with machine learning dipole moment

We used the LAMMPS package [94] to perform (DPMD) simulations combined with ML dipole moments for evaluating the dielectric properties of PG and PPGs. After initial configurations were generated from 10 ns CMD simulations, we performed a 200 ps equilibration, from which production runs of 2 or 4 ns and 20 ns were carried out. The WCs are sampled every 2.5 and 10 fs, respectively. All the DPMD simulations were conducted in an *NVT* ensemble at various temperatures with a Nosé-Hoover thermostat, with an integration time step of 0.5 fs. Calculations were performed on 64 molecule systems for all the materials. Densities were determined from *NPT* calculations of 500 ps.

As the estimation of  $\varepsilon^\infty$  was not within the scope of this work, we evaluated it from the square of the refractive index  $n$ , using the relation  $\varepsilon^\infty = n^2$ . The experimental values [95,96] of  $n = 1.43$  for PG and  $n = 1.45$  for PPG were used.

## IV. RESULTS AND DISCUSSION

### A. Propylene glycol

We first evaluate the accuracy of the trained ML dipole models and potentials. Figure 3 shows that the predicted dipole moments by our ML models align excellently with the DFT reference data for all the bond types. We randomly sampled 1000 validation structures from a 20 ps AIMD trajectory at 300 K. The bond dipoles increase on the order of CC, CH, and COH, with average values of 0.1, 0.9, and 2.0 D, respectively. The bond dipole moment of 1 D corresponds to about 0.1 Å of the displacement of WC. In the case of the CC bond, the WC is located near the BC due to symmetry, resulting in a small bond dipole. In contrast, the WC associated with CH bonds is located closer to the H atom than the C atom. Table I presents the root mean square error (RMSE)

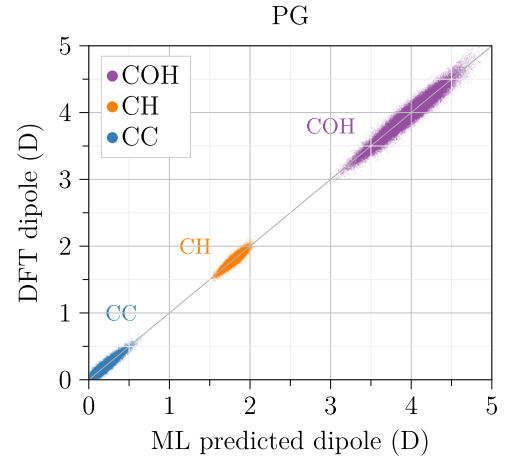


FIG. 3. Learning accuracy of ML bond dipoles of PG. The blue, orange, and purple dots represent the absolute values of the CC, CH, and COH bond dipoles, respectively.

for each bond, showing that the COH model provides slightly better accuracy than the sum of the CO, lone pair, and OH models. The newly conceived COH model can achieve comparable accuracy while reducing computational cost, making it particularly advantageous for long-time and large-scale calculations. In the following calculations, we calculate dipole moments using the COH model as described in Eq. (7), unless otherwise stated.

Figure 4 compares the calculated densities over the temperature range of 240–360 K with experimental values [97,98] to assess the accuracy of the trained ML potential. The boiling point of PG is approximately 460 K, towards which the density gradually decreases. At 300 K, the simulated density of 1.05 g/cm<sup>3</sup> closely matches the experimental density of 1.03 g/cm<sup>3</sup> [97] with a relative error of 1.9%. Our ML potential accurately reproduces the experimental values across a wide range of temperatures, albeit with a slight overestimation. At 380 K, the ML potential yields 0.993 g/cm<sup>3</sup> and the experimental density is 0.912 g/cm<sup>3</sup>, with the relative error reaching 8.9%. Recent ML studies on water have reported similar relative errors [85,99]. The good accuracy is because

TABLE I. RMSE [D] of ML dipole models for PG and PG2. The CO, O, and OH models were trained for reference purposes and were not used for spectrum calculations. The CO+Olp+OH and CO+Olp+CO represents the COH and COC dipoles calculated from these three models, respectively.

RMSE [D]	PG	PG2
CC	0.038	0.033
CH	0.031	0.027
COH	0.070	0.066
COC		0.077
CO	0.031	0.032
Olp	0.056	0.052
OH	0.023	0.023
CO+Olp+OH	0.072	0.071
CO+Olp+CO		0.080

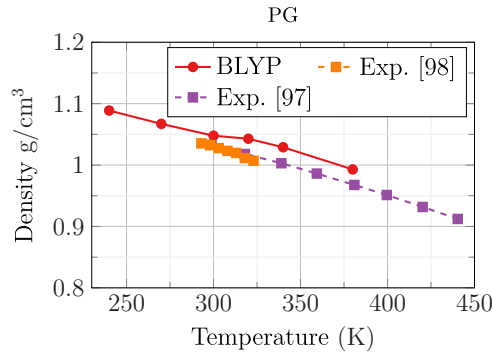


FIG. 4. Calculated density of PG from 240 to 360 K with experimental values from Sun *et al.* [97] and Khattab *et al.* [98] ranging from 293 to 440 K.

active sampling enabled us to include diverse structures spanning a broad range of temperatures and densities in the training data.

After confirming the high accuracy of the trained ML dipole and potential models, we studied the dielectric properties of PG. Figure 5 shows the calculated dielectric function in the THz to the far-IR region at three temperatures: 240, 270, and 300 K, with experimental values at 300 K [57]. Each spectrum was calculated from five independent 2 ns trajectories. Our calculations are in good agreement with the experimental values. The spectra are highly complex, characterized by a broad peak around  $50\text{ cm}^{-1}$  and another around  $600\text{ cm}^{-1}$  as the main features, with some sharp peaks between 200 and  $500\text{ cm}^{-1}$ . The peak around  $50\text{ cm}^{-1}$  is often referred to as the VDOS peak, as the total VDOS also has a peak at the same frequency [57,62]. The VDOS peak has been studied in relation to the boson peak in the supercooled or glassy states [100–103]. The temperature dependence of the spectra is small above  $400\text{ cm}^{-1}$ , while a concavity emerges in the low-frequency region with reduced temperatures, as the orientational relaxation peak in the GHz range shifts to lower frequencies at reduced temperatures [48].

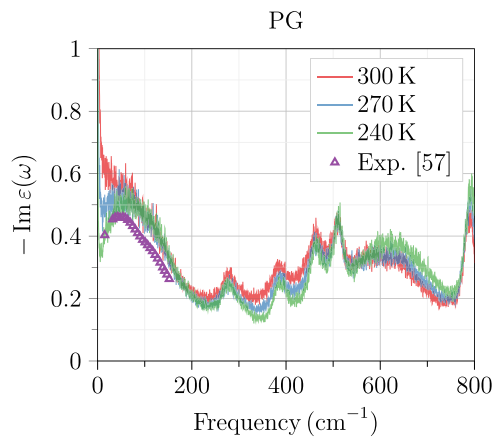


FIG. 5. Calculated imaginary part of dielectric functions of PG at three different temperatures: 240, 270, and 300 K with experimental values at 300 K [57]. The spectra were calculated from five independent 2 ns trajectories for each temperature, and smoothed using the moving average method.

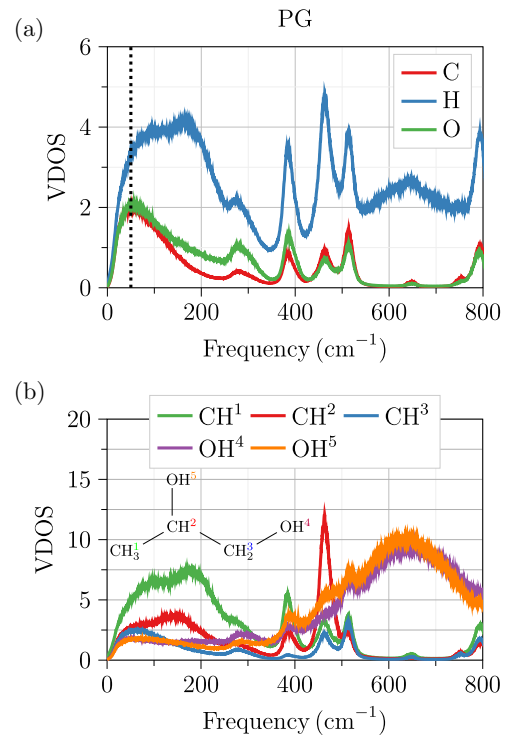


FIG. 6. (a) Calculated VDOS of carbon, oxygen, and hydrogen at 240 K. The position of the VDOS peak observed in the experimental dielectric function [57] is indicated by the black dashed line. (b) Calculated VDOS for hydrogen, decomposed according to its chemical environment.

To identify the origin of the multiple peaks in the THz region, Fig. 6(a) presents the calculated VDOS for each atomic species at 240 K. The VDOS was computed using the final 200 ps of the 2 ns trajectories used for calculating the dielectric function. As with the dielectric function, we observed sharp peaks at 280, 390, 460, and  $520\text{ cm}^{-1}$ , which are discussed in Appendix A. While the broad peak around  $600\text{ cm}^{-1}$  is primarily due to hydrogen motion, the low-frequency peak around  $100\text{ cm}^{-1}$  shows contributions from all the atomic species. The carbon and hydrogen peak near  $50\text{ cm}^{-1}$  called the VDOS peak, while the hydrogen shows a broader peak up to about  $180\text{ cm}^{-1}$ . Figure 6(b) further illustrates the VDOS for different types of hydrogen, revealing that all the types of hydrogen contributed to the VDOS peak at  $50\text{ cm}^{-1}$ , and the alkyl hydrogens are responsible for the higher frequencies up to  $200\text{ cm}^{-1}$ . On the other hand, the  $600\text{ cm}^{-1}$  peak is attributed to the hydroxyl hydrogens. This has been observed in other hydrogen-bonded molecular liquids, such as water [11] and methanol [104], and is ascribed to the librational (vibrational) motion of the hydroxyl hydrogen atoms. Figure 7 compares the absorption spectra of both deuterated and normal PG and shows that the prominent absorption peak at  $600\text{ cm}^{-1}$  in normal PG is redshifted to approximately  $500\text{ cm}^{-1}$  in deuterated PG, leading us to conclude that the peak is indeed due to the libration.

Figure 8(a) displays the dielectric function in the GHz frequency range, calculated at three temperatures: 240, 270, and 300 K, with experimental values at 270, 300, and 340 K

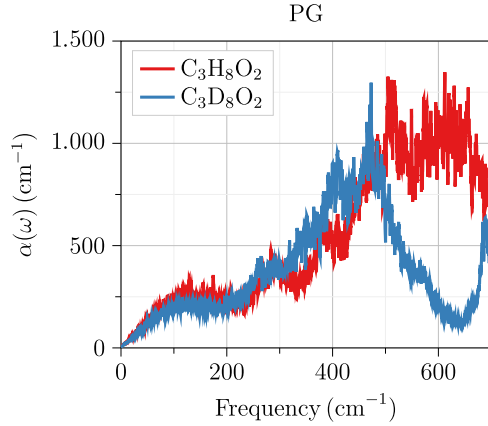


FIG. 7. Calculated absorption spectra of PG (red) and deuterated PG (blue) at 300 K. In the legend, H represents normal hydrogen, while D denotes deuterium.

[48]. These results were obtained by averaging five independent 20 ns MD trajectories, which far exceeds the timescales accessible by AIMD, highlighting the extended capabilities of the ML potentials and dipole moments. The frequency range corresponds to the high-frequency part of the orientational relaxation peak. In the case of PG, the orientational relaxation peak consists of a single peak; however, experimental data can be well-fitted using two Havriliak-Negami (HN) functions, with the low-frequency side referred to as the  $\alpha$  process and the high-frequency side as the  $\beta$  process [57,105]. The  $\alpha$  process is an orientation relaxation involving multiple molecules, whereas  $\beta$  processes originate from several physical origins, including the JG  $\beta$  process due to intermolecular interactions [106]. At 300 K, the peak frequency of the  $\alpha$  process, determined by fitting with the HN function, is located at  $0.013 \text{ cm}^{-1}$  (0.4 GHz) [57]. Our calculations accurately reproduce the experimental behavior that the peak position shifts significantly towards lower frequencies as the temperature decreases. As mentioned, a separation between the temperature-independent VDOS peak and the temperature-dependent  $\beta$  process occurs at low temperature, causing a concavity in the spectrum at around  $4 \text{ cm}^{-1}$ . Quantitatively, the results at 270 K closely match the experimental values at 300 K. This minor discrepancy likely arises from approximations involving the choice of the exchange-correlation functionals or neglecting nuclear quantum effects [36,107].

To estimate the impact of intermolecular interactions on the dielectric function, we decomposed the total dielectric function into intra- and intermolecular components. The total dipole moment of the system can be expressed as the sum of the molecular dipoles as  $\mathbf{M}(t) = \sum_i \boldsymbol{\mu}_i^{\text{mol}}(t)$ , and the dipole autocorrelation function can be calculated as the sum of the intramolecular and intermolecular correlation functions as

$$\begin{aligned} \langle \mathbf{M}(0) \cdot \mathbf{M}(t) \rangle &= \sum_i \langle \boldsymbol{\mu}_i^{\text{mol}}(0) \cdot \boldsymbol{\mu}_i^{\text{mol}}(t) \rangle \\ &+ \sum_{i \neq j} \langle \boldsymbol{\mu}_i^{\text{mol}}(0) \cdot \boldsymbol{\mu}_j^{\text{mol}}(t) \rangle. \end{aligned} \quad (27)$$

The total dielectric function can be divided into contributions from intramolecular and intermolecular interactions:

$$\begin{aligned} \varepsilon''(\omega) &= \frac{\omega}{6\varepsilon_0 k_B T V} \int_{-\infty}^{\infty} \left( \sum_i \langle \boldsymbol{\mu}_i^{\text{mol}}(0) \cdot \boldsymbol{\mu}_i^{\text{mol}}(t) \rangle \right. \\ &\quad \left. + \sum_{i \neq j} \langle \boldsymbol{\mu}_i^{\text{mol}}(0) \cdot \boldsymbol{\mu}_j^{\text{mol}}(t) \rangle \right) e^{-i\omega t} dt \end{aligned} \quad (28)$$

$$= \varepsilon''_{\text{intra}}(\omega) + \varepsilon''_{\text{inter}}(\omega). \quad (29)$$

Figure 8(b) shows the dielectric function at 300 K, decomposed into intra- and intermolecular components, in which we have discovered two key features. First, the intermolecular component sharply increases in the low-frequency region, as observed in water [5,6]. Recent experiments have been revealing that the  $\alpha$  process in hydrogen-bonded liquids is imputed to not a single-molecule orientational relaxation, but a relaxation of the hydrogen-bond network involving multiple molecules [108–110], and our calculations suggest that this is also true for PG. Second, the intermolecular-component exhibits a small peak around  $100 \text{ cm}^{-1}$ , while the intramolecular-component peaks near  $40 \text{ cm}^{-1}$ . Koda *et al.* [57] experimentally studied the dielectric spectra of liquid PG at room temperature, observing a prominent peak at  $50 \text{ cm}^{-1}$  and a small shoulder at  $120 \text{ cm}^{-1}$ , attributing the latter to intermolecular interactions. Our discovered peak in the intermolecular-component is located at nearly the same frequency as the experimentally observed one, providing theoretical support that this peak is due to correlations of intermolecular dipole moments. For hydrogen-bonded liquid molecules, a broad intermolecular peak in the THz region is generally attributed to hydrogen-bond stretching. In the case of water, the intermolecular part exhibits a significant peak at  $200 \text{ cm}^{-1}$ , the magnitude of which exceeds that of the intramolecular part. The intermolecular peak we found is considerably smaller than that of the intramolecular part, and investigating the cause of this discrepancy remains a subject for future investigation. Additionally, we observe that the libration motion at  $600 \text{ cm}^{-1}$  is predominantly explained by the intramolecular component, similar to other hydrogen-bonded liquids [5,46]. This indicates that the libration motion of hydroxyl hydrogen rarely induces dipole moments in neighbor molecules, unlike hydrogen-bond stretching motions.

Figure 9 shows the power spectra of  $r_{\text{OO}}$  and  $\mathbf{e}_{\text{OH}}$ , where  $r_{\text{OO}}$  represents the shortest intermolecular oxygen-oxygen distance, reflecting hydrogen bond stretching motions, and  $\mathbf{e}_{\text{OH}}$  denotes the unit direction vector of the OH bonds, corresponding to hydrogen motions. These spectra were calculated from 2 ns trajectories at 240 K. The  $\mathbf{e}_{\text{OH}}$  spectrum exhibits a prominent peak around  $600 \text{ cm}^{-1}$ , corresponding to the position of the libration peak. In contrast, the  $r_{\text{OO}}$  spectrum shows a significant peak around  $100 \text{ cm}^{-1}$ , which is associated with both the VDOS peak and the intermolecular interaction peak. Therefore, intermolecular hydrogen bonding plays a major role in the VDOS peak, even though it is not distinctly visible in the VDOS spectra in Fig. 6(a).

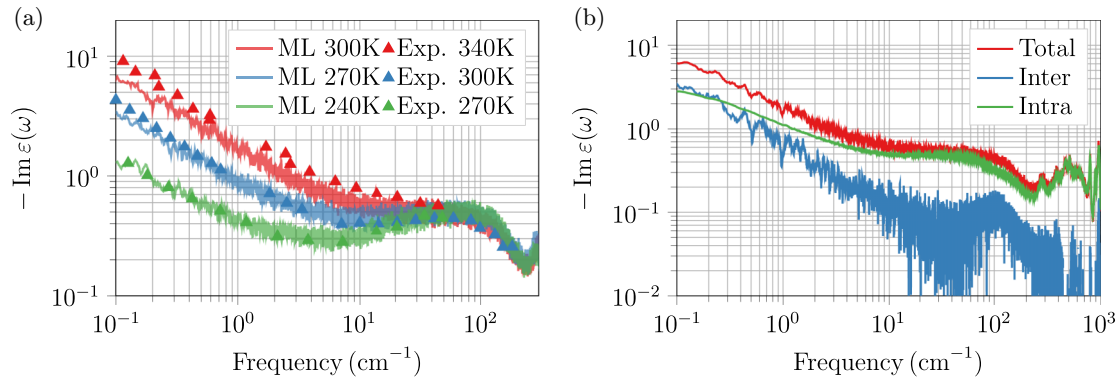


FIG. 8. (a) Calculated imaginary part of dielectric functions of PG (lines) in logarithmic scale at three different temperature: 240 (green), 270 (blue), and 300 K (red). The experimental values (symbols) are taken from Kohler *et al.* [48] at 270, 300, and 340 K, and Koda *et al.* [57] at 300 K. The spectra were calculated from five independent 20 ns trajectories for each temperature, and smoothed using the moving average method. (b) The total (red), intramolecular (green), and intermolecular (blue) components of the calculated imaginary part of dielectric functions of PG at 300 K according to Eq. (29). The intermolecular part peaks at  $100 \text{ cm}^{-1}$ , while the intramolecular part peaks at  $50 \text{ cm}^{-1}$ , corresponding to the VDOS peak.

### B. Oligomers

We examined the transferability of the chemical bond-based ML model using PPGs of varying chain lengths. We trained the ML dipole models using PG2, which, unlike PG, contains a COC segment (ether bond) and provides ideal training data for broader applications across PPGs. The model trained on PG2 was then applied to PG3, PG4, PG6, PG8, and PG12 to assess its accuracy and dielectric properties. Table I summarizes the RMSE of PG2 models applied to PG2 validation data, confirming that the prediction accuracy is almost identical to that of the PG model. The COH and COC models provide slightly better accuracy than the sum of the CO, lone pair, and OH models, confirming that our new approach is also effective for PG2.

Figure 10(a) illustrates the robust predictive performance of the PG2 model in estimating bond dipoles across PG oligomers. For validation, we randomly selected 1000 data points from each PG3, PG4, PG6, PG8, and PG12, and we compared the ML predictions to reference DFT calculations. The magnitude of each bond dipole remained nearly consistent, regardless of chain length. Figure 10(b) shows the

prediction accuracy as RMSE for each chain length. The model exhibited the highest accuracy for  $n = 2$ , with only a slight decline in precision as  $n$  increased. The accuracy is marginally lower for COC and CC bonds than for CH and COH bonds, which is likely due to electron delocalization as the chain length increases. These results corroborate that the PG2-trained model retains its accuracy and transferability, even when applied to various PPGs not referenced in the training.

Figure 11 compares calculated molecular dipoles in the liquid phase at several chain lengths with the experimental value of liquid PG at 298 K [65]. Error bars represent the standard deviations. The computed average dipole moment of PG was 3.6 D, which closely agreed with the experimental value of 3.2 D [65]. The calculated molecular dipoles in the liquid phase were about 1 D larger than the experimental values of the gas phase from Ref. [111], which is a well-known phenomenon for hydrogen-bonded molecules [46,112]. Our analysis further reveals that the dipole moment in the liquid phase also increases slightly with chain length. Given that the COH bond dipole does not significantly change with chain length, the increase in this dipole is likely caused by fluctuations in the dipole of the alkyl groups in either the main or side chains.

Figure 12(a) demonstrates that the predicted dielectric function of PG2 closely matches the experimental values [48], confirming the reliability of the trained ML models. The intensity of the orientation relaxation of PG2 is clearly smaller than that of PG. The observed temperature discrepancy with the experiment is consistent with that of PG in Fig. 8(a), suggesting that approximations such as the exchange-correlation functional and neglecting quantum effects may influence the relaxation dynamics of PG and PG2 similarly. Figure 12(b) compares the THz dielectric function of PG and PG2. The peak intensity of the libration of PG2 at  $600 \text{ cm}^{-1}$  is smaller than that of PG and is buried in the narrow peaks of local vibrational modes. This is because the number of OH groups in PG2 is half that of PG, reducing the generated dipole moments of the libration. On the other hand, the VDOS peak of PG2 is only slightly smaller than that of PG and has a very

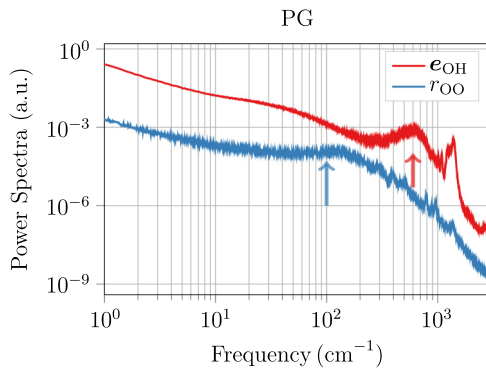


FIG. 9. Calculated power spectra of  $r_{\text{OO}}$  and  $e_{\text{OH}}$  according to Eq. (16) of PG at 240 K. The peak positions of the intermolecular mode at  $100 \text{ cm}^{-1}$  and the librational mode at  $600 \text{ cm}^{-1}$  are indicated with blue and red arrows, respectively.



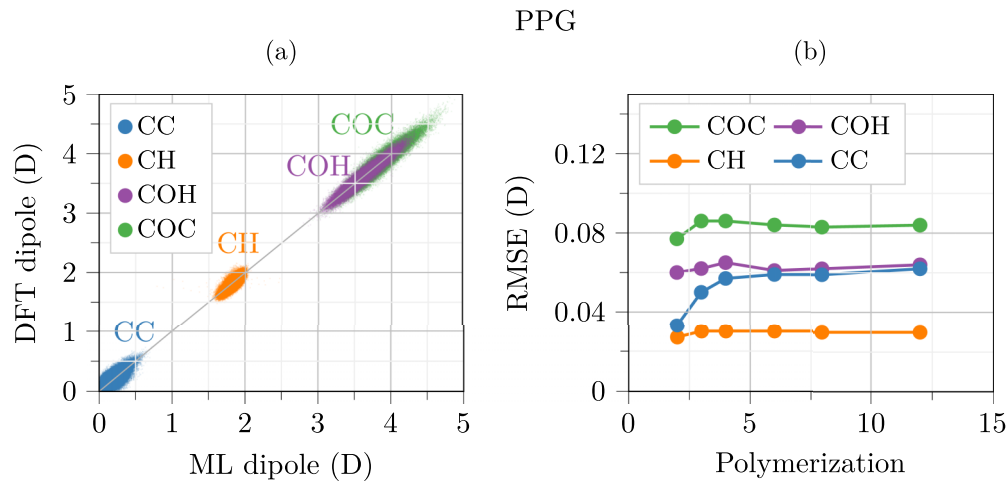


FIG. 10. (a) Learning accuracy of ML bond dipoles of PG2, PG3, PG4, PG6, PG8, and PG12. The blue, orange, purple, and green dots represent the absolute values of the CC, CH, COH, and COC bond dipoles, respectively. (b) The chain length dependence of the prediction accuracy in terms of RMSE.

similar shape. The VDOS peak, therefore, originates not only from OH groups but also from other atoms. Figure 13 shows that the VDOS peak of the dielectric function of PG12, using the ML potential and dipole moments trained on PG2 training data, agrees well with experimental values [57]. This confirms that the PG2 ML models can reliably predict the dielectric properties of PPGs with longer chain lengths, which are not referenced during training. The spectrum was computed from five independent 2 ns trajectories with 64 molecules, in a total of 7872 atoms. Notably, the peak position is almost identical regardless of the chain length, while the peak intensity decreases with increasing chain length. The decrease in intensity may be due to the reduction in the density of the OH groups with increasing chain length.

## V. CONCLUSION

Through a study of the dielectric properties of PG and PPG, we validated the transferability and effectiveness of our bond-based ML dipole moment scheme combined with

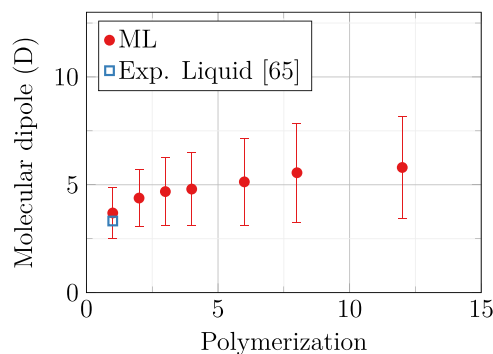


FIG. 11. The average molecular dipole moments of PPGs with various chain lengths. For each system, 1000 molecular dipole moments were randomly sampled from 200 ps DPMD calculations of 64 molecule systems. The experimental dipole moment of PG in the liquid phase (blue) is taken from Ref. [65].

ML potentials. In this scheme, we assigned WCs to each chemical bond, and we trained ML models to predict the WC for each bond type. We adopted a slightly modified approach from the previous study to improve accuracy while reducing computational costs, which is suitable for long-time and large-scale calculations. Furthermore, to achieve extended

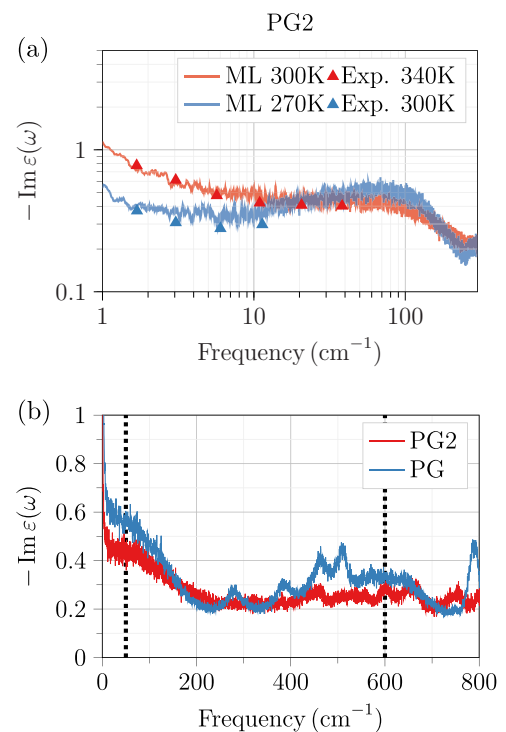


FIG. 12. (a) Calculated dielectric function of PG2 at 300 (red) and 270 K (blue) together with the experimental values at 340 (red triangle) and 300 K (blue triangle) [48]. The spectrum was calculated from five independent 4 ns trajectories with the moving average method. (b) Calculated dielectric function of PG2 (red) and PG (blue) at 300 K. The vertical dotted lines correspond to the peak position of the VDOS and libration peak at 50 and 600 cm<sup>-1</sup>, respectively.

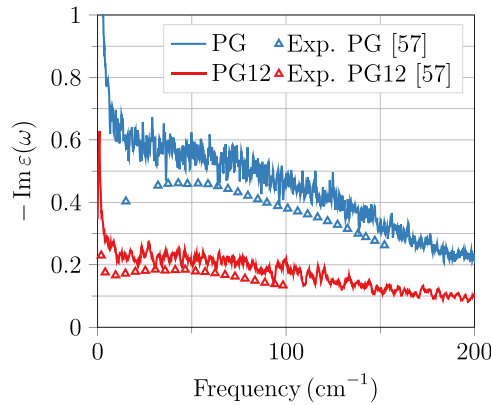


FIG. 13. The calculated imaginary part of the dielectric functions of PG and PG12 at 300 K with experimental data for PG and PG12 at 300 K [57]. The data of PG are the same as that shown in Fig. 8.

simulation times of up to 20 ns, the ML potentials were trained using active sampling.

We first investigated the dielectric properties of PG, which is the first detailed analysis from first-principles to the best of our knowledge. Our developed ML dipole models demonstrated high accuracy, and successfully reproduced the dielectric function in both the THz and GHz regions. Notably, the GHz dielectric function was calculated using 20 ns MD trajectories, a timescale beyond the reach of AIMD. In the THz region, the dominant features are the VDOS peak at  $50 \text{ cm}^{-1}$  and the hydroxyl hydrogen libration peak at  $600 \text{ cm}^{-1}$ . The VDOS peak reflects overall molecular vibrations involving carbon, hydrogen, and oxygen atoms and is attributed to intramolecular components of the dielectric function. We also found a shoulder at  $100 \text{ cm}^{-1}$  in the dielectric function of the intermolecular component, which was previously found experimentally. Our analysis of the oxygen-oxygen interatomic power spectrum suggests that the hydrogen bond stretching may contribute significantly to the VDOS peak. In the GHz range, the intermolecular components become dominant at lower frequencies below  $0.4 \text{ cm}^{-1}$ .

We then applied the ML dipole models, trained on PG2 data, to PPGs with longer chain lengths which were not included in the training data. The models accurately predicted the bond dipoles of PPGs regardless of the chain length. The molecular dipole moment of liquid PPGs gradually increases with chain length. Furthermore, we calculated the dielectric function of PG12, demonstrating good agreement with experimental data. Considering that the structure of PG12 was not included in the training data, our calculation underscores the high transferability of our approach. We expect the current approach to be the first step toward developing a universal bond dipole model for various molecular systems.

#### ACKNOWLEDGMENTS

This research was funded by a JST-Mirai Program Grant No. JPMJMI20A1, a MEXT Quantum Leap Flagship Program (MEXT Q-LEAP) Grant No. JPMXS0118067246, Japan, and JSR Corporation via JSR-UTokyo Collaboration Hub, CURIE. The computations in this study have been

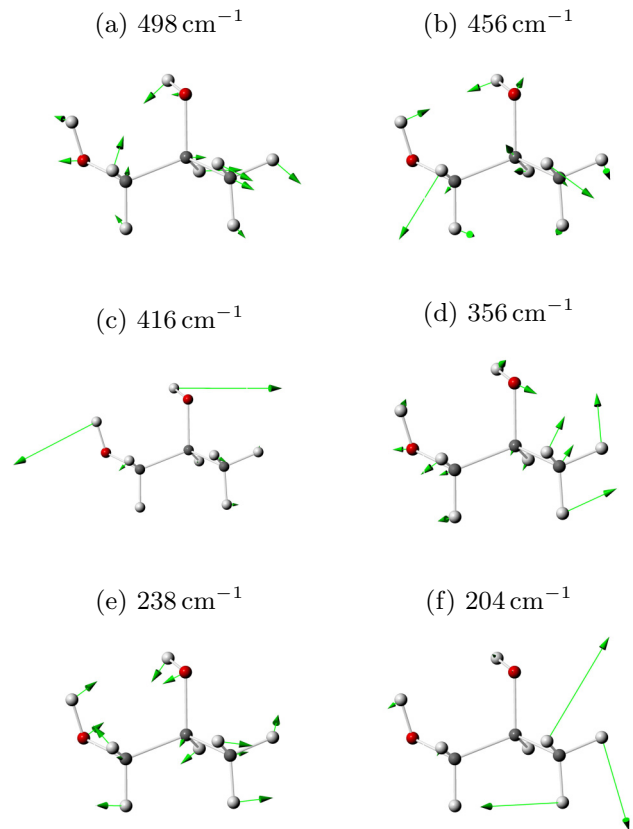


FIG. 14. Calculated vibrational modes of the gas phase PG, the frequencies of which range from 200 to  $500 \text{ cm}^{-1}$ . Oxygen, carbon, and hydrogen are represented by red, gray, and white spheres, respectively. The green arrows represent the magnitude and direction of the eigenvectors of the vibration modes.

conducted using computational resources of the supercomputer Fugaku provided by the RIKEN Center for Computational Science (ProjectID: hp220331, hp230124, and hp240148) and the facility of the Supercomputer Center, the Institute for Solid State Physics, the University of Tokyo.

#### APPENDIX A: VIBRATIONAL ANALYSIS OF GAS PHASE PG

Here, we study the origin of several sharp peaks in VDOS of Fig. 6(a) at 280, 390, 460, and  $520 \text{ cm}^{-1}$ , which show contributions from all C, H, and O atoms. These peaks are local vibrational modes and can be analyzed using gas phase calculations [57]. We employed VASP [113,114] for structural relaxation and finite-difference vibrational analysis with the BLYP functional. The plane-wave energy cutoff was set to 600 eV, with an energy convergence threshold of  $1 \times 10^{-9} \text{ eV}$ . We placed one PG molecule in the cubic cell with the lattice parameter of  $20 \text{ \AA}$ , with only the  $\Gamma$  point used for electronic integration. Figure 14 shows the six calculated vibrational modes, the frequencies of which range from 200 to  $600 \text{ cm}^{-1}$ . Among these, the  $204 \text{ cm}^{-1}$  vibration corresponds to the rotational motion of alkyl hydrogens, and the  $416 \text{ cm}^{-1}$  vibration is attributed to the librational motion of hydroxyl hydrogens, which do not appear in Fig. 6(a) as these

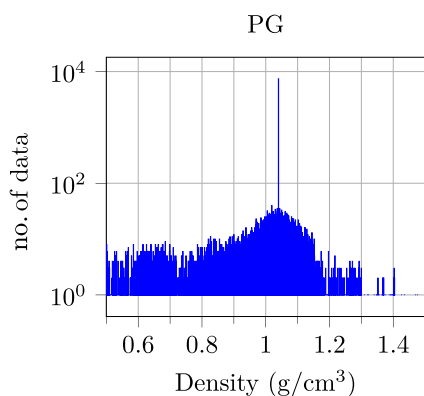


FIG. 15. The density distribution of the final dataset of PG.

two modes only have significant contribution from hydrogen atoms. Therefore, the remaining four modes, representing vibrational motions of the main molecular chain, correspond to sharp peaks observed in Fig. 6(a).

#### APPENDIX B: THE FEATURES OF THE FINAL DATASET OF PG

We summarized the features of the final dataset of PG. Figure 15 shows the density distribution of the

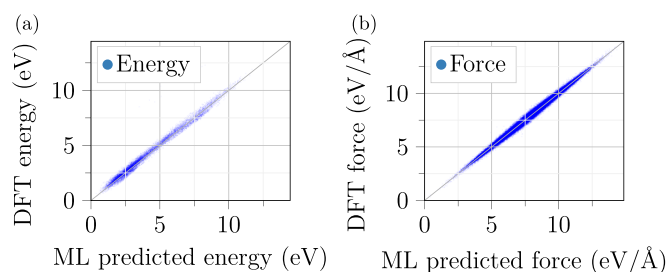


FIG. 16. The (a) energy and (b) force accuracy of the ML potential of PG. The final dataset of PG was used.

final dataset of PG. The density distribution ranges broadly from approximately 0.5 to 1.4 g/cm<sup>3</sup>. The most abundant structures are found around 1.05 g/cm<sup>3</sup>, the density used to generate the initial structures. The active sampling procedure improved the robustness of the ML potentials by incorporating structures across a wide range of densities, enabling an accurate performance over a broad temperature range.

Figure 16 shows that the ML potentials accurately predict the energies and forces of the final PG dataset. The broad distribution of energies and forces confirms that the dataset comprises diverse structures.

- [1] G. Fugallo, B. Rousseau, and M. Lazzeri, Infrared reflectance, transmittance, and emittance spectra of MgO from first principles, *Phys. Rev. B* **98**, 184307 (2018).
- [2] T. Amano, T. Yamazaki, R. Akashi, T. Tadano, and S. Tsuneyuki, Lattice dielectric properties of rutile TiO<sub>2</sub>: First-principles anharmonic self-consistent phonon study, *Phys. Rev. B* **107**, 094305 (2023).
- [3] T. Kulschewski and J. Pleiss, A molecular dynamics study of liquid aliphatic alcohols: Simulation of density and self-diffusion coefficient using a modified OPLS force field, *Mol. Simul.* **39**, 754 (2013).
- [4] A. Mishra, L. Chen, Z. Li, K.-i. Nomura, A. Krishnamoorthy, S. Fukushima, S. C. Tiwari, R. K. Kalia, A. Nakano, R. Ramprasad, G. Sotzing, Y. Cao, and P. Vashishta, Computational framework for polymer synthesis to study dielectric properties using polarizable reactive molecular dynamics, *Comput. Mater. Sci.* **228**, 112340 (2023).
- [5] S. Carlson, F. N. Brüning, P. Loche, D. J. Bonthuis, and R. R. Netz, Exploring the absorption spectrum of simulated water from MHz to infrared, *J. Phys. Chem. A* **124**, 5599 (2020).
- [6] C. Hölzl, H. Forbert, and D. Marx, Dielectric relaxation of water: Assessing the impact of localized modes, translational diffusion, and collective dynamics, *Phys. Chem. Chem. Phys.* **23**, 20875 (2021).
- [7] J. H. Ryu, J. W. Yu, T. J. Yoon, and W. B. Lee, Understanding the dielectric relaxation of liquid water using neural network potential and classical pairwise potential, *J. Mol. Liq.* **397**, 124054 (2024).
- [8] J. A. Lemkul, J. Huang, B. Roux, and A. D. J. MacKerell, An empirical polarizable force field based on the classical drude oscillator model: Development history and recent applications, *Chem. Rev.* **116**, 4983 (2016).
- [9] P. Cieplak, F.-Y. Dupradeau, Y. Duan, and J. Wang, Polarization effects in molecular mechanical force fields, *J. Phys.: Condens. Matter* **21**, 333102 (2009).
- [10] T. Binninger, D. Saraç, L. Marsh, T. Picard, M.-L. Doublet, and C. Raynaud, AMOEBA polarizable force field for molecular dynamics simulations of glyme solvents, *J. Chem. Theor. Comput.* **19**, 1023 (2023).
- [11] D. Sharma, B. Das, and A. Chandra, Terahertz spectrum of water at varying temperatures from 260 to 340 K: Contributions from permanent and induced dipole correlations at different length scales, *J. Phys. Chem. B* **127**, 6714 (2023).
- [12] R. Car and M. Parrinello, Unified approach for molecular dynamics and density-functional theory, *Phys. Rev. Lett.* **55**, 2471 (1985).
- [13] J.-W. Handgraaf, T. S. van Erp, and E. J. Meijer, *Ab initio* molecular dynamics study of liquid methanol, *Chem. Phys. Lett.* **367**, 617 (2003).
- [14] J.-W. Handgraaf, E. J. Meijer, and M.-P. Gaigeot, Density-functional theory-based molecular simulation study of liquid methanol, *J. Chem. Phys.* **121**, 10111 (2004).
- [15] C. C. Wang, J. Y. Tan, and L. H. Liu, *Ab initio* molecular dynamics study of temperature and pressure-dependent infrared dielectric functions of liquid methanol, *AIP Adv.* **7**, 035115 (2017).
- [16] R. D. King-Smith and D. Vanderbilt, Theory of polarization of crystalline solids, *Phys. Rev. B* **47**, 1651 (1993).

- [17] N. Marzari and D. Vanderbilt, Maximally localized generalized Wannier functions for composite energy bands, *Phys. Rev. B* **56**, 12847 (1997).
- [18] N. Marzari, A. A. Mostofi, J. R. Yates, I. Souza, and D. Vanderbilt, Maximally localized Wannier functions: Theory and applications, *Rev. Mod. Phys.* **84**, 1419 (2012).
- [19] N. Sieffert, M. Bühl, M.-P. Gaigeot, and C. A. Morrison, Liquid methanol from DFT and DFT/MM molecular dynamics simulations, *J. Chem. Theor. Comput.* **9**, 106 (2013).
- [20] V. L. Deringer, A. P. Bartók, N. Bernstein, D. M. Wilkins, M. Ceriotti, and G. Csányi, Gaussian process regression for materials and molecules, *Chem. Rev.* **121**, 10073 (2021).
- [21] J. Behler and M. Parrinello, Generalized neural-network representation of high-dimensional potential-energy surfaces, *Phys. Rev. Lett.* **98**, 146401 (2007).
- [22] H. Wang, L. Zhang, J. Han, and W. E, DeePMD-kit: A deep learning package for many-body potential energy representation and molecular dynamics, *Comput. Phys. Commun.* **228**, 178 (2018).
- [23] J. Gilmer, S. S. Schoenholz, P. F. Riley, O. Vinyals, and G. E. Dahl, Neural message passing for quantum chemistry, in *Proceedings of the 34th International Conference on Machine Learning* (PMLR, 2017), pp. 1263–1272.
- [24] A. Musaelian, S. Batzner, A. Johansson, L. Sun, C. J. Owen, M. Kornbluth, and B. Kozinsky, Learning local equivariant representations for large-scale atomistic dynamics, *Nat. Commun.* **14**, 579 (2023).
- [25] M. Gastegger, J. Behler, and P. Marquetand, Machine learning molecular dynamics for the simulation of infrared spectra, *Chem. Sci.* **8**, 6924 (2017).
- [26] M. Veit, D. M. Wilkins, Y. Yang, R. A. DiStasio, and M. Ceriotti, Predicting molecular dipole moments by combining atomic partial charges and atomic dipoles, *J. Chem. Phys.* **153**, 024113 (2020).
- [27] A. E. Sifain, N. Lubbers, B. T. Nebgen, J. S. Smith, A. Y. Lokhov, O. Isayev, A. E. Roitberg, K. Barros, and S. Tretiak, Discovering a transferable charge assignment model using machine learning, *J. Phys. Chem. Lett.* **9**, 4495 (2018).
- [28] R. Beckmann, F. Briec, C. Schran, and D. Marx, Infrared spectra at coupled cluster accuracy from neural network representations, *J. Chem. Theor. Comput.* **18**, 5492 (2022).
- [29] D. P. Metcalf, A. Jiang, S. A. Spronk, D. L. Cheney, and C. D. Sherrill, Electron-passing neural networks for atomic charge prediction in systems with arbitrary molecular charge, *J. Chem. Inf. Model.* **61**, 115 (2021).
- [30] M. Thürlmann, L. Bösel, and S. Riniker, Learning atomic multipoles: Prediction of the electrostatic potential with equivariant graph neural networks, *J. Chem. Theor. Comput.* **18**, 1701 (2022).
- [31] T. W. Ko, J. A. Finkler, S. Goedecker, and J. Behler, A fourth-generation high-dimensional neural network potential with accurate electrostatics including non-local charge transfer, *Nat. Commun.* **12**, 398 (2021).
- [32] P. Bleiziffer, K. Schaller, and S. Riniker, Machine learning of partial charges derived from high-quality quantum-mechanical calculations, *J. Chem. Inf. Model.* **58**, 579 (2018).
- [33] T. Bereau, R. A. DiStasio, Jr., A. Tkatchenko, and O. A. von Lilienfeld, Non-covalent interactions across organic and biological subsets of chemical space: Physics-based potentials parametrized from machine learning, *J. Chem. Phys.* **148**, 241706 (2018).
- [34] K. Yao, J. E. Herr, D. W. Toth, R. Mckintyre, and J. Parkhill, The TensorMol-0.1 model chemistry: A neural network augmented with long-range physics, *Chem. Sci.* **9**, 2261 (2018).
- [35] O. T. Unke and M. Meuwly, PhysNet: A neural network for predicting energies, forces, dipole moments, and partial charges, *J. Chem. Theor. Comput.* **15**, 3678 (2019).
- [36] A. Krishnamoorthy, K.-i. Nomura, N. Baradwaj, K. Shimamura, P. Rajak, A. Mishra, S. Fukushima, F. Shimojo, R. Kalia, A. Nakano, and P. Vashishta, Dielectric constant of liquid water determined with neural network quantum molecular dynamics, *Phys. Rev. Lett.* **126**, 216403 (2021).
- [37] L. Zhang, M. Chen, X. Wu, H. Wang, W. E, and R. Car, Deep neural network for the dielectric response of insulators, *Phys. Rev. B* **102**, 041121(R) (2020).
- [38] G. M. Sommers, M. F. C. Andrade, L. Zhang, H. Wang, and R. Car, Raman spectrum and polarizability of liquid water from deep neural networks, *Phys. Chem. Chem. Phys.* **22**, 10592 (2020).
- [39] L. Zhang, H. Wang, M. C. Muniz, A. Z. Panagiotopoulos, R. Car, and W. E, A deep potential model with long-range electrostatic interactions, *J. Chem. Phys.* **156**, 124107 (2022).
- [40] P. Xie, Y. Chen, W. E, and R. Car, *Ab initio* multi-scale modeling of ferroelectrics: The case of PbTiO<sub>3</sub>, [arXiv:2205.11839](https://arxiv.org/abs/2205.11839).
- [41] B. Yang, P. Xie, and R. Car, Deuteration removes quantum dipolar defects from KDP crystals, *npj Comput. Mater.* **10**, 241 (2024).
- [42] V. Kapil, D. M. Wilkins, J. Lan, and M. Ceriotti, Inexpensive modeling of quantum dynamics using path integral generalized Langevin equation thermostats, *J. Chem. Phys.* **152**, 124104 (2020).
- [43] R. Hou, Y. Quan, and D. Pan, Dielectric constant of supercritical water in a large pressure–temperature range, *J. Chem. Phys.* **153**, 101103 (2020).
- [44] A. Gao and R. C. Remsing, Self-consistent determination of long-range electrostatics in neural network potentials, *Nat. Commun.* **13**, 1572 (2022).
- [45] M. Cools-Ceuppens, J. Dambre, and T. Verstraelen, Modeling electronic response properties with an explicit-electron machine learning potential, *J. Chem. Theor. Comput.* **18**, 1672 (2022).
- [46] T. Amano, T. Yamazaki, and S. Tsuneyuki, Chemical bond based machine learning model for dipole moment: Application to dielectric properties of liquid methanol and ethanol, *Phys. Rev. B* **110**, 165159 (2024).
- [47] L. De Francesco, M. Cutroni, and A. Mandanici, Broad-band dielectric spectroscopy of some alcohols down to the glass transition temperature  $T_g$ , *Philos. Mag. B* **82**, 625 (2002).
- [48] M. Köhler, P. Lunkenheimer, Y. Goncharov, R. Wehn, and A. Loidl, Glassy dynamics in mono-, di- and tri-propylene glycol: From the  $\alpha$ - to the fast  $\beta$ -relaxation, *J. Non-Cryst. Solids* **356**, 529 (2010).
- [49] E. Ikada and M. Ashida, Liquid properties of oligomers. Comparison of relaxational properties of propylene glycol oligomers with those of ethylene glycol oligomers, *Colloid Polymer Sci.* **264**, 602 (1986).
- [50] I.-S. Park, K. Saruta, and S. Kojima, Dielectric relaxation and calorimetric measurements of glass transition in the



- glass-forming dihydroxyl alcohols, *J. Phys. Soc. Jpn.* **67**, 4131 (1998).
- [51] T. M. Usacheva, N. V. Lifanova, V. I. Zhuravlev, and V. K. Matveev, A dielectric study of the structure of propylene glycol, *Russ. J. Phys. Chem. A* **84**, 1194 (2010).
- [52] Y.-L. Kao, C.-J. Hsieh, and M.-H. Li, Static dielectric constants of aqueous glycol solutions of ethylene, diethylene, triethylene, tetraethylene, propylene, and dipropylene, *J. Chem. Eng. Jpn.* **40**, 385 (2007).
- [53] S. Pawlus, S. Hensel-Bielowka, M. Paluch, R. Casalini, and C. M. Roland, Hydrogen bonding and secondary relaxations in propylene glycol trimer, *Phys. Rev. B* **72**, 064201 (2005).
- [54] P. A. Chalikwar, A. R. Deshmukh, and A. C. Kumbharkhane, Dielectric relaxation of Tripropylene glycol–water mixture using time domain reflectometry, *Phys. Chem. Liq.* **55**, 410 (2017).
- [55] L. P. Singh and G. Sharma, Dielectric spectroscopy investigation of relaxation processes in the low-frequency regime and validity of the Stokes–Einstein–Nernst/Stokes–Einstein–Debye relation in poly(propylene glycol), *Macromol. Res.* **31**, 33 (2023).
- [56] S. Capaccioli, R. Casalini, M. Lucchesi, G. Lovicu, D. Prevosto, D. Pisignano, G. Romano, and P. A. Rolla, Influence of the end groups on dynamics of propylene glycol oligomers studied by wideband dielectric spectroscopy, *J. Non-Cryst. Solids* **307**, 238 (2002).
- [57] S. Koda, T. Mori, and S. Kojima, Broadband terahertz dynamics of propylene glycol monomer and oligomers, *J. Mol. Struct.* **1126**, 127 (2016).
- [58] M. E. Baur and W. H. Stockmayer, Dielectric relaxation in liquid polypropylene oxides, *J. Chem. Phys.* **43**, 4319 (1965).
- [59] R. J. Sengwa, R. Chaudhary, and S. C. Mehrotra, The study of dielectric relaxation in propylene glycol–poly(propylene glycol) mixtures, *Polymer* **43**, 1467 (2002).
- [60] E. S. C. Ferreira, I. V. Voroshylova, V. A. Koverga, C. M. Pereira, and M. N. D. S. Cordeiro, New force field model for propylene glycol: Insight to local structure and dynamics, *J. Phys. Chem. B* **121**, 10906 (2017).
- [61] A. Brodin, L. M. Torell, P. Ahlström, and G. Wahnström, Raman scattering from systems of linear chain molecules (poly(propylene oxide)) of different lengths: A comparison with molecular dynamics simulations, *Philos. Mag. B* **77**, 709 (1998).
- [62] P. Ahlström, G. Wahnström, P. Carlsson, S. Schantz, A. Brodin, F. Maurer, and L. Torell, Low-frequency vibrations in monomers, dimers and polymers of propylene glycol, *Philos. Mag. B* **77**, 699 (1998).
- [63] W. L. Jorgensen, D. S. Maxwell, and J. Tirado-Rives, Development and testing of the OPLS all-atom force field on conformational energetics and properties of organic liquids, *J. Am. Chem. Soc.* **118**, 11225 (1996).
- [64] R. J. Sengwa, A comparative dielectric study of ethylene glycol and propylene glycol at different temperatures, *J. Mol. Liq.* **108**, 47 (2003).
- [65] T. Vishwam, N. K. S. P. S. Sarma, S. S. Sastry, and V. R. K. Murthy, Dielectric relaxation studies of acetonitrile/propylene glycol and their binary mixtures, *Indian J. Pure Appl. Phys.* **55**, 403 (2017).
- [66] J. Zeng, D. Zhang, D. Lu, P. Mo, Z. Li, Y. Chen, M. Rynik, L. Huang, Z. Li, S. Shi, Y. Wang, H. Ye, P. Tuo, J. Yang, Y. Ding, Y. Li, D. Tisi, Q. Zeng, H. Bao, Y. Xia *et al.*, DeePMD-kit v2: A software package for deep potential models, *J. Chem. Phys.* **159**, 054801 (2023).
- [67] M. Neumann and O. Steinhauser, Computer simulation and the dielectric constant of polarizable polar systems, *Chem. Phys. Lett.* **106**, 563 (1984).
- [68] J. Cardona, M. B. Sweatman, and L. Lue, Molecular dynamics investigation of the influence of the hydrogen bond networks in ethanol/water mixtures on dielectric spectra, *J. Phys. Chem. B* **122**, 1505 (2018).
- [69] E. Hecht, *Optics* (Pearson Education, 2017).
- [70] M. Sharma, R. Resta, and R. Car, Intermolecular dynamical charge fluctuations in water: A signature of the H-Bond network, *Phys. Rev. Lett.* **95**, 187401 (2005).
- [71] R. Ramírez, T. López-Ciudad, P. Kumar P, and D. Marx, Quantum corrections to classical time-correlation functions: Hydrogen bonding and anharmonic floppy modes, *J. Chem. Phys.* **121**, 3973 (2004).
- [72] J. Liu, J. Lan, and X. He, Toward high-level machine learning potential for water based on quantum fragmentation and neural networks, *J. Phys. Chem. A* **126**, 3926 (2022).
- [73] M. J. Abraham, T. Murtola, R. Schulz, S. Páll, J. C. Smith, B. Hess, and E. Lindahl, GROMACS: High performance molecular simulations through multi-level parallelism from laptops to supercomputers, *SoftwareX* **1-2**, 19 (2015).
- [74] L. Martínez, R. Andrade, E. G. Birgin, and J. M. Martínez, PACKMOL: A package for building initial configurations for molecular dynamics simulations, *J. Comput. Chem.* **30**, 2157 (2009).
- [75] J. Wang, R. M. Wolf, J. W. Caldwell, P. A. Kollman, and D. A. Case, Development and testing of a general amber force field, *J. Comput. Chem.* **25**, 1157 (2004).
- [76] A. Jakalian, D. B. Jack, and C. I. Bayly, Fast, efficient generation of high-quality atomic charges. AM1-BCC model: II. Parameterization and validation, *J. Comput. Chem.* **23**, 1623 (2002).
- [77] J. Wang, W. Wang, P. A. Kollman, and D. A. Case, Automatic atom type and bond type perception in molecular mechanical calculations, *J. Mol. Graph. Modell.* **25**, 247 (2006).
- [78] A. W. S. da Silva and W. F. Vranken, ACPYPE - AnteChamber PYthon Parser interfacE, *BMC Res. Notes* **5**, 367 (2012).
- [79] P. Zarzycki and B. Gilbert, Temperature-dependence of the dielectric relaxation of water using non-polarizable water models, *Phys. Chem. Chem. Phys.* **22**, 1011 (2020).
- [80] <https://github.com/CPMD-code>.
- [81] C. Lee, W. Yang, and R. G. Parr, Development of the Colle-Salvetti correlation-energy formula into a functional of the electron density, *Phys. Rev. B* **37**, 785 (1988).
- [82] A. D. Becke, Density-functional exchange-energy approximation with correct asymptotic behavior, *Phys. Rev. A* **38**, 3098 (1988).
- [83] S. Grimme, Semiempirical GGA-type density functional constructed with a long-range dispersion correction, *J. Comput. Chem.* **27**, 1787 (2006).
- [84] S. Goedecker, M. Teter, and J. Hutter, Separable dual-space Gaussian pseudopotentials, *Phys. Rev. B* **54**, 1703 (1996).
- [85] P. Montero de Hijes, C. Dellago, R. Jinnouchi, B. Schmiedmayer, and G. Kresse, Comparing machine learning

- potentials for water: Kernel-based regression and Behler–Parrinello neural networks, *J. Chem. Phys.* **160**, 114107 (2024).
- [86] N. Matsumura, Y. Yoshimoto, T. Yamazaki, T. Amano, T. Noda, N. Ebata, T. Kasano, and Y. Sakai, Generator of neural network potential for molecular dynamics: Constructing robust and accurate potentials with active learning for nanosecond-scale simulations, *J. Chem. Theory Comput.* **21**, 3832 (2025).
- [87] S. Nosé, A unified formulation of the constant temperature molecular dynamics methods, *J. Chem. Phys.* **81**, 511 (1984).
- [88] M. Parrinello and A. Rahman, Crystal structure and pair potentials: A molecular-dynamics study, *Phys. Rev. Lett.* **45**, 1196 (1980).
- [89] I.-B. Magdău, D. J. Arismendi-Arrieta, H. E. Smith, C. P. Grey, K. Hermansson, and G. Csányi, Machine learning force fields for molecular liquids: Ethylene Carbonate/Ethyl Methyl Carbonate binary solvent, *npj Comput. Mater.* **9**, 146 (2023).
- [90] Y. Zhang, H. Wang, W. Chen, J. Zeng, L. Zhang, H. Wang, and W. E, DP-GEN: A concurrent learning platform for the generation of reliable deep learning based potential energy models, *Comput. Phys. Commun.* **253**, 107206 (2020).
- [91] A. Narayan, B. Berger, and H. Cho, Assessing single-cell transcriptomic variability through density-preserving data visualization, *Nat. Biotechnol.* **39**, 765 (2021).
- [92] H. Ibayashi, T. M. Razakh, L. Yang, T. Linker, M. Olguin, S. Hattori, Y. Luo, R. K. Kalia, A. Nakano, K.-i. Nomura, and P. Vashishta, Allegro-Legato: Scalable, fast, and robust neural-network quantum molecular dynamics via sharpness-aware minimization, in *High Performance Computing. ISC High Performance 2023*, edited by A. Bhatele, J. Hammond, M. Baboulin, and C. Kruse, Lecture Notes in Computer Science, Vol. 13948 (Springer Nature Switzerland, Cham, 2023), pp. 223–239.
- [93] T. Amano, <https://github.com/ToAmano/MLWC>.
- [94] A. P. Thompson, H. M. Aktulga, R. Berger, D. S. Bolintineanu, W. M. Brown, P. S. Crozier, P. J. in't Veld, A. Kohlmeyer, S. G. Moore, T. D. Nguyen, R. Shan, M. J. Stevens, J. Tranchida, C. Trott, and S. J. Plimpton, LAMMPS - a flexible simulation tool for particle-based materials modeling at the atomic, meso, and continuum scales, *Comput. Phys. Commun.* **271**, 108171 (2022).
- [95] U. E. N. C. f. E. Assessment, *CRC Handbook of Chemistry and Physics* (CRC press, Boca Raton, 2009).
- [96] T. Vishwam, S. Shihab, V. R. K. Murthy, H. S. Tiong, and S. Sreehari Sastry, Microwave dielectric relaxation spectroscopy study of propylene glycol/ethanol binary mixtures: Temperature dependence, *Spectrochim. Acta Pt. A* **179**, 74 (2017).
- [97] T. Sun and A. S. Teja, Density, viscosity and thermal conductivity of aqueous solutions of propylene glycol, dipropylene glycol, and tripropylene glycol between 290 K and 460 K, *J. Chem. Eng. Data* **49**, 1311 (2004).
- [98] I. S. Khattab, F. Bandarkar, M. Khoubnasabjafari, and A. Jouyban, Density, viscosity, surface tension, and molar volume of propylene glycol + water mixtures from 293 to 323 K and correlations by the Jouyban–Acree model, *Arab. J. Chem.* **10**, S71 (2017).
- [99] B. Cheng, E. A. Engel, J. Behler, C. Dellago, and M. Ceriotti, *Ab initio* thermodynamics of liquid and solid water, *Proc. Natl. Acad. Sci. USA* **116**, 1110 (2019).
- [100] U. Schneider, P. Lunkenheimer, R. Brand, and A. Loidl, Dielectric and far-infrared spectroscopy of glycerol, *J. Non-Cryst. Solids* **235**, 173 (1998).
- [101] Y. Yomogida, Y. Sato, R. Nozaki, T. Mishina, and J. Nakahara, Comparative study of boson peak in normal and secondary alcohols with terahertz time-domain spectroscopy, *J. Phys. B* **405**, 2208 (2010).
- [102] Y. Yomogida, Y. Sato, K. Yamakawa, R. Nozaki, T. Mishina, and J. Nakahara, Comparative dielectric study of pentanol isomers with terahertz time-domain spectroscopy, *J. Mol. Struct.* **970**, 171 (2010).
- [103] M. Kabeya, T. Mori, Y. Fujii, A. Koreeda, B. W. Lee, J.-H. Ko, and S. Kojima, Boson peak dynamics of glassy glucose studied by integrated terahertz-band spectroscopy, *Phys. Rev. B* **94**, 224204 (2016).
- [104] H. Torii, Intermolecular charge fluxes and terahertz spectral features of liquid methanol, *J. Mol. Liq.* **390**, 123111 (2023).
- [105] K. Grzybowska, S. Pawlus, M. Mierzwa, M. Paluch, and K. L. Ngai, Changes of relaxation dynamics of a hydrogen-bonded glass former after removal of the hydrogen bonds, *J. Chem. Phys.* **125**, 144507 (2006).
- [106] K. L. Ngai, P. Lunkenheimer, C. León, U. Schneider, R. Brand, and A. Loidl, Nature and properties of the Johari–Goldstein  $\beta$ -relaxation in the equilibrium liquid state of a class of glass-formers, *J. Chem. Phys.* **115**, 1405 (2001).
- [107] J. Xu, C. Zhang, L. Zhang, M. Chen, B. Santra, and X. Wu, Isotope effects in molecular structures and electronic properties of liquid water via deep potential molecular dynamics based on the SCAN functional, *Phys. Rev. B* **102**, 214113 (2020).
- [108] J. S. Hansen, A. Kisliuk, A. P. Sokolov, and C. Gainaru, Identification of structural relaxation in the dielectric response of water, *Phys. Rev. Lett.* **116**, 237601 (2016).
- [109] P. Sillrén, A. Matic, M. Karlsson, M. Koza, M. Maccarini, P. Fouquet, M. Götz, Th. Bauer, R. Gulich, P. Lunkenheimer, A. Loidl, J. Mattsson, C. Gainaru, E. Vynokur, S. Schildmann, S. Bauer, and R. Böhmer, Liquid 1-propanol studied by neutron scattering, near-infrared, and dielectric spectroscopy, *J. Chem. Phys.* **140**, 124501 (2014).
- [110] R. Böhmer, C. Gainaru, and R. Richert, Structure and dynamics of monohydroxy alcohols—Milestones towards their microscopic understanding, 100 years after Debye, *Phys. Rep.* **545**, 125 (2014).
- [111] E. Ikada, H. Fukushima, and T. Watanabe, Dielectric properties of oligomers. VII. Low-molecular-weight propylene glycols, *J. Polym. Sci.* **17**, 1789 (1979).
- [112] M. Jorge, J. R. B. Gomes, and A. W. Milne, Self-consistent electrostatic embedding for liquid phase polarization, *J. Mol. Liq.* **322**, 114550 (2021).
- [113] G. Kresse and J. Furthmüller, Efficient iterative schemes for *ab initio* total-energy calculations using a plane-wave basis set, *Phys. Rev. B* **54**, 11169 (1996).
- [114] G. Kresse and D. Joubert, From ultrasoft pseudopotentials to the projector augmented-wave method, *Phys. Rev. B* **59**, 1758 (1999).